

## New Features Observed in Self-Absorption-Corrected X-ray Fluorescence Spectra for Ni Complexes with Uncertainties

Ryan M. Trevorah, Christopher T. Chantler,\* and Martin J. Schalken

Cite This: *J. Phys. Chem. A* 2020, 124, 1634–1647

Read Online

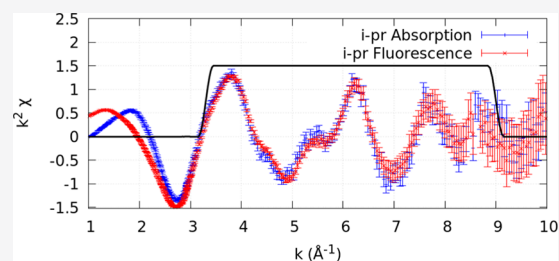
ACCESS |

Metrics &amp; More

Article Recommendations

Supporting Information

**ABSTRACT:** We present a new technology for analyzing the molecular structure and in particular subtle conformational differences in Ni complexes using X-ray absorption spectroscopy (XAS), enabling tighter and more robust constraints of structure and dynamic bond lengths. Self-absorption and attenuating effects have a large impact in fluorescence X-ray absorption spectroscopy (XAS), compromising accuracy and insight in structural and advanced analyses. We correct for these dominant systematic effects. We investigate nickel(II) complexes, that is, bis(*N*-*n*-propyl-salicylaldiminato) nickel(II), “*n*-pr”, and bis(*N*-*i*-propyl-salicylaldiminato) nickel(II), “*i*-pr”, in 15 mM solutions with 0.1% w/w Ni. One is “square-planar” and one is “tetrahedral”, with identical coordination numbers. We identify two key sources of uncertainty and provide robust estimates for them, reflecting the quality of the data, and provide meaningful estimates of  $\chi_r^2$  suitable for hypothesis testing. We apply significance and model testing for fluorescence data, with direct uncertainty estimates. Two new peaks are revealed in the X-ray absorption fine structure (XAFS) at  $k \approx 4.4$  and  $5.4 \text{ \AA}^{-1}$ . The high intrinsic accuracy of our processed data allows these features to be well modeled and yields deeper potential insight. Three important notions in the field are addressed: resolvability of shell radii, estimation of the number of independent data points in least-squares or Bayesian analysis, and the effect of uncertainties on the determined structure and the determinability of key structural parameters. Conventional XAFS fitting requires a  $k_{\min}$  and a  $k_{\max}$ . The origin of these limits is explained from the data, in a quantitative manner. Being able to distinguish the isomers spectroscopically and structurally places strong demands on the data, the uncertainties, and the model interpretation, and this article reports success in this subtle structural identification. Two nearby shells—the innermost two shells—are identified quantitatively, well below the conventional aliasing limit. This illustrates the application of new technology to gain new insight.



## INTRODUCTION

X-ray absorption fine structure (XAFS) is caused by back-scattering and self-interference of the wave function of an emitted photoelectron within the material near the emitting atom. The potential of this technique is often limited by poorly quantified experimental uncertainties or untreated systematic effects.<sup>1–3</sup> Fluorescence measurement<sup>4</sup> is a particularly useful technique for dilute systems<sup>4,5</sup> and is very commonly used for modern experiments. For XAFS measurements conducted using fluorescence detection, it is particularly challenging to obtain accurate statistical uncertainties compared with experiments conducted in “transmission mode”, and most published spectra are reported with no experimental uncertainty. Instead, uncertainties are routinely estimated by looking at residual fluctuations remaining in fully processed transformed data.<sup>6</sup>

A common perception is that one typically collects (fluorescence) XAFS data for long enough so that counting statistics from the data do not dominate the uncertainties in the structural parameters, which may be dominated by theoretical limitations, data processing systematic effects, or correlated fitting uncertainties. While these play a great role, it is increasingly important to be able to assess them using standard error (SE) analysis. Post facto normalization of

goodness-of-fit measures should use processed raw data uncertainties, however accurate, and should be evaluated following  $\chi_r^2$  standard uncertainty analysis.

In a recent publication, our research group presented a methodology for correcting the dominant systematic distortion in fluorescence XAFS (attenuation and self-absorption),<sup>7</sup> and the results showed excellent agreement when presented as  $[\mu/\rho]$  versus energy. In the crystalline form, the complexes considered in this work have been found to have local metal environments with approximate tetrahedral and square-planar coordination geometries.<sup>8,9</sup> A previous publication by our group examined dilute frozen solutions of these complexes using transmission-mode XAFS<sup>10</sup> and further refined the coordination geometry as part of that study.<sup>11</sup> Recently, a study was conducted on this system by transmission analysis with careful propagation of data information and uncertainty.<sup>12</sup> This system therefore provides an excellent test of fluorescent

Received: November 12, 2019

Revised: December 18, 2019

Published: January 29, 2020

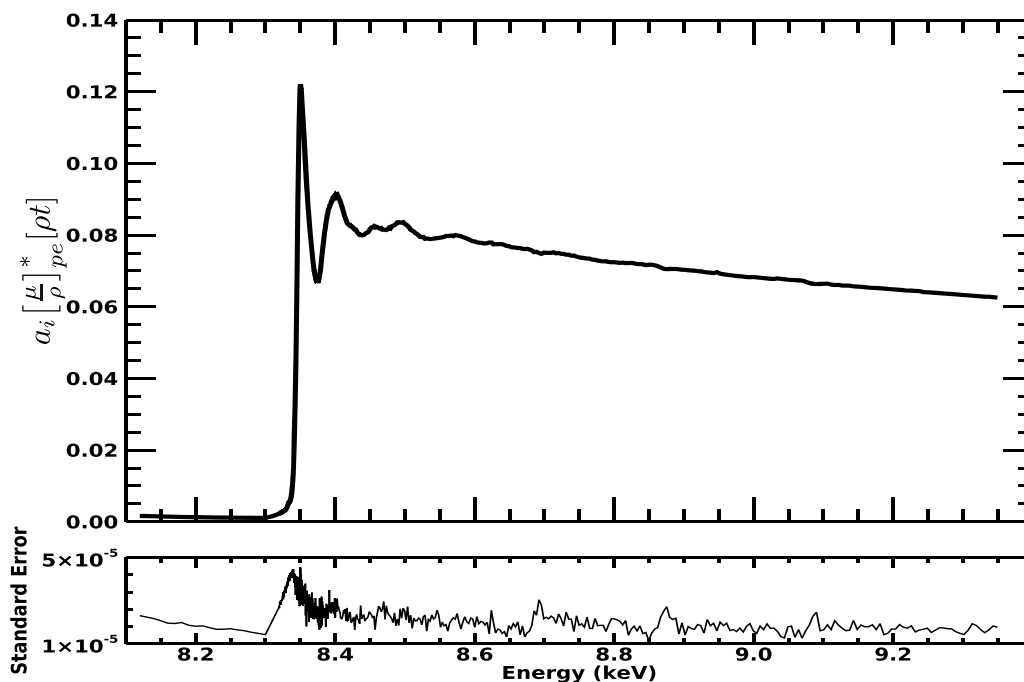


**Figure 1.** Result of averaging 33 spectra of the *n-pr* data set after self-absorption correction, now with particularly small standard uncertainty.

multipixel data and further demonstrates the merit of using complementary techniques to confirm molecular geometries.<sup>13,14</sup>

Fluorescence and transmission XAS measurements were simultaneously taken of two closely related organometallics: bis(*N-n*-propyl-salicylaldiminato) nickel(II), “*n-pr*”, and bis(*N-i*-propyl-salicylaldiminato) nickel(II), “*i-pr*”, at the Australian National Beamline Facility, Tsukuba, Japan. Next, 15 mM solutions of each complex were prepared using 60% butyronitrile + 40% acetonitrile as the solvent to avoid microcrystallization at cryostat temperatures, ca. 80 K. The concentrations of the solute were  $15.33 \pm 0.06$  and  $15.26 \pm 0.03$  mM, respectively, corresponding to approximately 0.1% w/w or 1000 ppm (parts per million) nickel in the sample. Sample (cell) thicknesses were  $1.9577 \pm 0.0017$  mm (*i-pr*) and  $1.981 \pm 0.002$  mm (*n-pr*) (Table 3, column 4, ref 10). A 36-element Ge planar detector (EURISYS EPIX 36-64-7-ER) was used to collect fluorescence. The detector contains  $6 \times 6$  channels forming a square area, with each pixel capturing an area of 8 mm  $\times$  8 mm. The central position of the detector is aligned to be  $\sim 45^\circ$  to the solution cell and  $\sim 90^\circ$  to the incident beam.

A detailed schematic of the transmission experiment with accurate distances can be found in Figure 5 of ref 10, with the fluorescence geometry given elsewhere (Figure 3 of ref 7). Previous XERT<sup>15</sup> and Hybrid<sup>10</sup> analyses have considered concentrated samples. The simultaneous data collection in both modes gives a critical comparison of fluorescence with transmission in a regime where both methods are fully competitive. The processing of the data to remove self-absorption and attenuation effects from the multipixel data<sup>7</sup> yields spectra and deposited tabulations with  $\left[\frac{\mu}{\rho}\right]$ -versus-*E*.

The current work is composed of three sections. The section **Uncertainties in XAFS** gives a brief experimental and processing background, investigates the effect of the correction of absorptive effects in fluorescence upon the fine oscillatory

structure, and explains the derivation of nonuniform pointwise uncertainties. These uncertainties transform in the data sets presented, according to conventional XAFS fitting approaches on different axes. This results in a natural *k*-range of analysis based on the data while considering the effective range of the theory and the model being fitted. This process enables observation of new XAFS features.

The second section, **Important Notions of Analysis**, addresses three important notions in the field: resolvability of shell radii, estimation of the number of independent data points in least-squares or Bayesian analysis, and the effect of uncertainties on the determined structure and the determinability of key structural parameters.

The third section, **Structural Investigation of Nickel Complexes**, investigates what quantitative information can be obtained from the fluorescence investigation using the nonuniform pointwise propagated uncertainties and how the results of structural analysis compare to previously published transmission XAFS results. Distinguishing one complex from the other spectroscopically and structurally places strong demands on the data, the uncertainties, and the model interpretation, as demonstrated by this subtle structural identification. The high intrinsic accuracy of the processed data allows these features to be well modeled, enables fitting of two nearby innermost shells accurately, and yields deeper potential insight.

## METHODS

**Uncertainties in XAFS.** *Variance Gives the Estimated Pointwise Uncertainty, Including Statistical and Several Systematic Uncertainties.* Fluorescence experimental setups include a multipixel detector and collect a separate spectrum for each pixel. These spectra are usually averaged before converting to  $\chi$  to begin structural analysis. The standard analysis methodology does not propagate measured experimental variance, thus discarding the information from the pointwise variance between the spectra collected by each pixel.

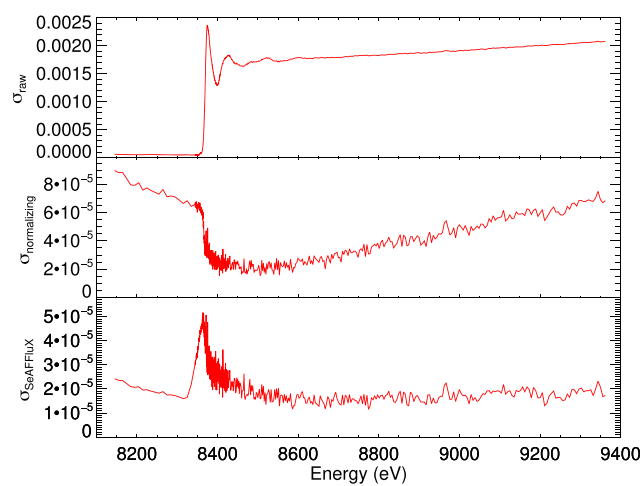
There is real information contained in this variance, including the number of independent parameters, and this is the most easily accessible insight into the statistical and systematic uncertainties in any experiment. Characterizing this variance allows the user to define a minimum baseline uncertainty in the absence of other sources of variance and systematic uncertainty. To generate this variance from raw multipixel data, they must be normalized and attenuation-corrected for each pixel. Otherwise,<sup>7</sup> the variance will be extremely large, resulting in a major overestimate of the statistical uncertainty from this source. By using, for example, a software package such as SeAFFluX,<sup>7</sup> the consistency of repeated information content by pixel or by energy is well-defined and the minimal variance is a fair representation of statistical noise and any time-, energy-, or pixel-dependent systematic shifts.

A simple example of systematic uncertainty is a bias in X-ray detection on one side of the detector compared to the other, from a misalignment of the fluorescence detector relative to your sample. This becomes apparent by inspecting the spread of spectra, grouped by the positions on the detector. Such an effect can be corrected for, for the systematic effect and geometry or by propagating the pointwise standard uncertainty between spectra through to later stages of analysis. Another common systematic distortion is uncalibrated detection efficiencies, yielding greatly differing amplitudes recorded by adjacent pixels. Statistical uncertainty is represented by random fluctuations of photon count or in the electronic readout or amplification of the detector itself.<sup>16,17</sup> Many processes can cause such systematic effects, including detector dead-time and pileup noise. Following this preanalysis, corrected spectra were averaged and a pointwise standard uncertainty was calculated and propagated (Figure 1). Previous investigations of these distortions in fluorescence spectra of XAFS required knowledge of the sample stoichiometry<sup>18</sup> or the energy dependence of the absorption coefficients,<sup>19</sup> or making a series of measurements at multiple angles.<sup>20</sup> Major surveys and developments have been made in this area by many researchers in pure and applied chemistry,<sup>21,22</sup> biological and medical science,<sup>23</sup> and earth sciences and engineering.<sup>24,25</sup>

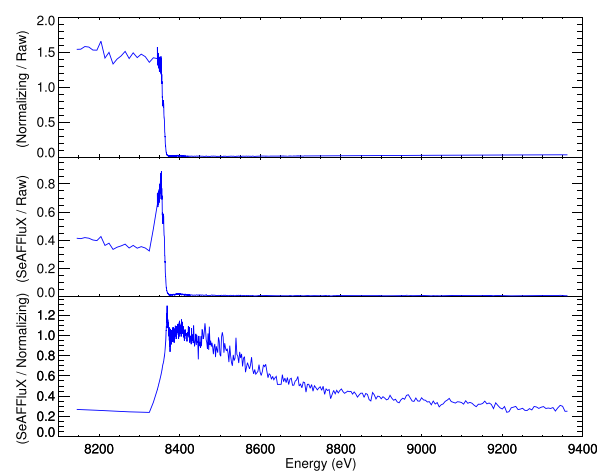
**Effect of Data Uncertainties on Modeling Structural Parameters and Uncertainties in  $\chi$ .** Care should be taken in the propagation of uncertainty when converting XAFS data from the scaled fluorescence signal  $\frac{I_f}{I_0}$  or  $\left[\frac{\mu}{\rho}\right]$  (mass absorption coefficient or mass attenuation coefficient) or  $\mu$  (linear absorption coefficient) to  $\chi$ , including propagation of correlated versus uncorrelated uncertainty and random versus systematic shifts.

Herein, variances from the collected (full) pixel array of the multipixel detector yield estimates of both the statistical uncertainty and the random systematic uncertainty. Figure 2 illustrates the great improvement this makes to the estimate of these uncertainties compared with simpler measures. Almost any estimate is preferred to the absence of an estimate. Careful data collection and analysis can define this at the  $10^{-5}$  level compared with the active orbital magnitude of  $a_i \left[\frac{\mu}{\rho}\right]_{pe}^* [\rho t] \sim 0.08 - 0.12$  (Figure 1), with an improvement

of a factor of 20–200 compared with uncorrected raw data. A significant source of uncertainty is introduced in the process of converting  $\mu$  to  $\chi$ , an unavoidable step toward structural analysis of any XAFS data set. Perhaps the simplest and most



(a)



(b)

**Figure 2.** Data uncertainty for the data set from the pixels uncorrected for self-absorption and attenuation; normalized; and corrected for self-absorption and attenuation. (a) Standard errors for the *i*-pr Ni complex: for the “raw” spectra (top), after correction for detector efficiency (middle), and after self-absorption correction with SeAFFluX (bottom). A “normalizing” method and our self-absorption correction reduce the standard error by orders of magnitude, although the distributions are markedly different. SeAFFluX produces the lowest standard error across the spectrum, a powerful demonstration of the model. (b) Comparison of the improvement in standard error relative to the raw spectra due to the normalizing method (top), after correcting for self-absorption using SeAFFluX (middle), and SeAFFluX versus the normalizing method (bottom). Both methods significantly reduce the variance. Uncalibrated detector efficiency is a major contribution to the variance. The self-absorption correction is far superior to the normalizing method, especially in the mid- to high-energy range.

widely used method involves background subtraction, edge estimation, and fitting a spline function through the original  $\mu$  data to isolate the oscillatory pattern in the XAFS data, together with glitch removal, data “selection”, and interpolation. This process introduces significant systematic uncertainty to the data set, quite difficult to quantify.<sup>12</sup>

For fluorescence data, we remove Bragg glitches (monochromator secondary reflections) or characterize them.<sup>7</sup> This

should not be needed in a well-designed transmission experiment but is inevitable in fluorescence data collection. These can be either characterized and corrected for or recognized and omitted in the determination of variance, either at some prior step or at this point in the analysis. Each of these alternatives is possible. Figure 3 indicates the corrected spectra.

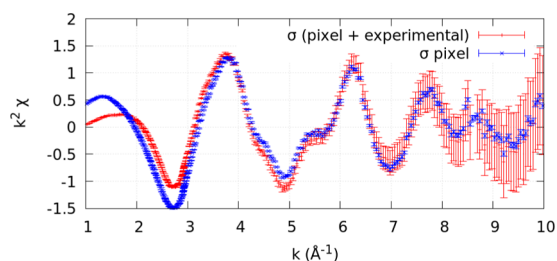


**Figure 3.** Comparison of uncertainty due to pixel-averaging (blue) and including quadrature estimates of errors (uncertainties) due to pathlength uncertainties (red).

*Estimation of Additional Known and Unknown Uncertainties and Their Propagation from  $\left[\frac{\mu}{\rho}\right]$  versus  $E$  to  $\chi$ ,  $k\chi$ ,  $k^2\chi$ , and  $k^3\chi$  versus  $k$ .* As noted,<sup>26</sup> “conventional methods to obtain  $\chi$  from the raw data make it very difficult to determine ‘experimental’ errors”. In the current case, uncertainties were estimated and recorded during the experiment for the air path

length as well as the kapton tape and silicone layer thicknesses. These are key parameters in any self-absorption and attenuation correction model, and so uncertainties in these quantities lead to an uncertainty in the final “corrected” spectra. To be clear, this is not simply a change to the overall scale, which would cancel out when converting to  $\chi$ , but an energy-dependent change, leading to different slopes in the final corrected spectra. In part, this is due in turn to uncertainties in the “standard” extraction of  $\chi$ , that is, the background removal, edge energy location or definition, above edge spline, or other empirical definitions of a smooth “atomic” reference background and ergo the extraction of the oscillations, amplitudes, and magnitudes. Hence, an uncertainty or systematic distortion manifests itself as a change in relative amplitude or offset in the  $\chi$ -versus- $k$  space. An uncertainty including this was generated by producing spectra using the range of experimental lengths and thicknesses and propagating these through the  $\chi$ -versus- $k$  extraction process. This was added in quadrature to the uncertainty from averaging the pixel spectra. This “path length” uncertainty is larger than that due to pixel-averaging in this example, at higher  $k$  (Figure 3). This path length uncertainty could be significantly reduced by increasing the accuracy of measurements of experimental geometry and is a comment neither on the quality of data produced by the experiment nor on that transformed by SeAFFluX. The structural oscillations in the  $\chi$  spectrum tend to decrease dramatically with an increase in  $k$ , so it is common to analyze spectra scaled by  $k$ ,  $k^2$ , or  $k^3$ . Figure

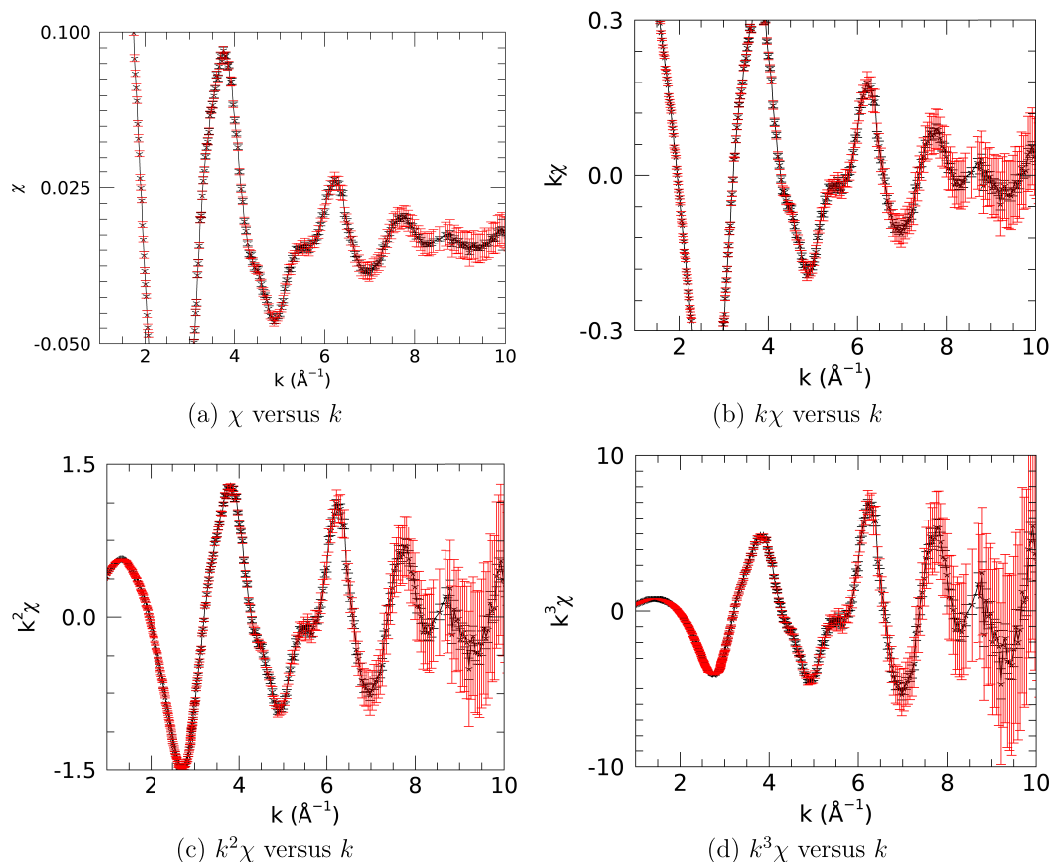


**Figure 4.** Plots of  $k^n\chi$  versus  $k$  for the fluorescence spectra. The black spectrum includes the uncertainty from pointwise variance between pixels, whereas the red spectrum includes uncertainty from both the pointwise variance and geometric uncertainties. The information content is the highest at low  $k$ , and absolute and relative noise increases with  $k$  in a natural manner but with independent pointwise estimates.

4 illustrates the correct scaling of uncertainties from  $\chi$  versus  $k$  to, for example,  $k^2\chi$  versus  $k$ . In all cases, the noise and uncertainty increase with  $k$ . This experiment was optimized in spacing and dwell time; however, since the beamline is a second-generation one rather than a third-generation one, it remains flux-limited, especially at high  $k$ . Thus, maximal information content occurs at lower  $k$ .

In principle, one should be able to analyze the full transmission or fluorescence spectrum directly, without transforming to the  $\chi$ -versus- $k$  space and hence introducing uncertainty with the edge energy, background subtraction, and spline. This is true and has been investigated<sup>27–30</sup> with some continued challenges; however, to date, the approach used almost universally is the one we discuss herein.

A cutoff value is conventionally chosen at high  $k$  somewhat arbitrarily, at a point where the data appears too noisy. This cutoff is enforced by a window function, most commonly a Hanning window. The methodology we present here of propagating uncertainty throughout the analysis highlights a key point in the analysis methodology (Figure 4). The relative noise, or the signal-to-noise ratio, is exactly the same in all plots; however, the cutoff of the Hanning window chosen is normally fully correlated with the choice of scale ( $k$ ,  $k^2$ ,  $k^3$ ).

Propagation and analysis using the uncertainty estimates mean that the choice of fitting on  $k\chi$ ,  $k^2\chi$ , or  $k^3\chi$  axes is not relevant because the fitting will be normalized by the equally scaled uncertainties in all cases. Additionally, the selection of the upper limit of the Hanning window can be both robust and arbitrary because the uncertainties naturally deprecate the significance of high- $k$  data points. Our methodology aims to accurately estimate the sources of experimental uncertainty and removes the need to arbitrarily decide on a high- $k$  cutoff value. The lower limit of a Hanning or fitting window has a quite different origin: limitations of the theory, of the model, and of the parameters such as  $\Delta E_0$ , meaning that fitting in the low- $k$  region yields a high  $\chi_r^2$ . Avoiding these theory, model, and fitting limitations implies the use of a low- $k$  window limit for fitting. A fitting window can be used in  $k$ -space or in  $r$ -space; the physical meaning is quite transparent in  $k$ -space.

**Observation of New XAFS Features.** Figure 5 presents the processed  $\chi$  fluorescence spectrum and overlays it on transmission results. Both data sets have rigorously defined defensible uncertainties. Hence, the significance of new

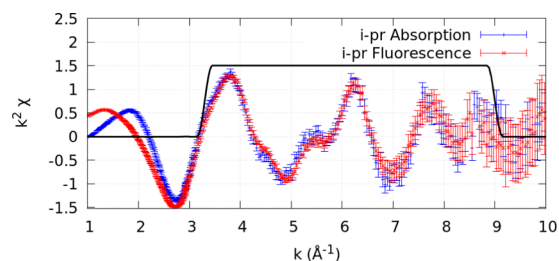


**Figure 5.** Fluorescence spectra overlaid with published transmission spectra.<sup>12</sup> The first peak within the Hanning window is in good agreement with the spectra. The transmission spectrum has a larger amplitude than the fluorescence spectrum in these regions. Features at  $k \sim 4.4$  and  $5.4 \text{ \AA}^{-1}$  are clear and were not well-defined or well-fitted in previous transmission analyses. This is partially due to smaller relative uncertainties in that region for the fluorescence data and partially due to the transmission analysis using too large a  $k$ -window (Figure 9).

features seen in the spectra can be assessed. We highlight two features seen in the fluorescence spectrum at around  $4.4$  and  $5.4 \text{ \AA}^{-1}$ , respectively. The uncertainties are relatively small in this region and significantly smaller than in the absorption data set reported previously. In hindsight, these two peaks can be seen in the absorption data<sup>10,12</sup> but were missed originally due to the large uncertainties, both by authors and by least-squared analysis. In the transmission data sets these features were not of major significance, and hence these spectral features were not fitted. An earlier study fitted the region<sup>12</sup> but did not fit nor model the features well because the uncertainties were too high. However, these features are now correctly represented and yield greater insight from the structural modeling and improved structural analysis. The clear identification of these extra features well above noise and statistical uncertainty enables significant improvement in structural and model analyses.

## ■ IMPORTANT NOTIONS OF ANALYSIS

**Minimum Atomic Radial Separations and “Nyquist-like” Prescriptions.** A real and pervading question is what information content can be gained from a spectrum, with or without uncertainties, and how this can define a structure to a higher level of accuracy and insight. We illustrate this in the current section with pure sine waves and a finite  $k$ -range of fitting, approximately matching that of our current data sets. We omit mean free path and thermal broadening but include a defined uniform Gaussian noise  $\sigma(\chi)$  to the spectrum, pointwise, as each data point is defined to be an independent data point. We then “estimate”, as part of the preparation for fitting the spectrum, a given noise or uncertainty estimate and fit accordingly (Figure 6). If we correctly estimate the same

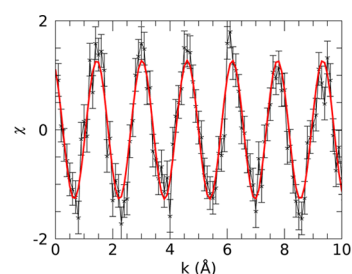


**Figure 6.** Simple pure sine wave simulation including pointwise normally distributed noise (black line) and fit (red), discussed in relation to normal statistical analysis and signal processing in Tables 1 and 2 and the text.

scale of Gaussian noise as the data, it should be no surprise that a model fit yields a  $\chi_r^2$  value close to unity. Conversely, also as expected, if our estimate is 5 times too large or 10 times too small, then the estimated  $\chi_r^2$  is increased or decreased by this error squared; the uncertainty on a particular parameter, say  $\sigma(R_j)$ , is scaled inversely to this. This confirms that, in the presence of a poor uncertainty estimate, the robust estimate of a parameter is  $\sigma(R_j)\sqrt{\chi_r^2}$  as known from standard statistical analysis (Table 1).

The spectrum can be very noisy, yet it can determine the radius of a shell or atomic scatterer as  $2.000 \pm 0.002 \text{ \AA}$  (Figure 6), with perhaps a 3% uncertainty on amplitude and a similar uncertainty on phase or phase offset while fitting over a  $k$ -range from 0 to  $10 \text{ \AA}^{-1}$ . In this illustration, parameters are made similar to real data presented later; one standard deviation

**Table 1. Illustration Demonstrating that Poorly Estimated Experimental Uncertainties Can Artificially Influence the Reported Uncertainty of the Model Parameters, Yielding Misleading Parameter Estimates, e.g.,  $\sigma(R_i)$ ; yet  $\sigma(R_i)\sqrt{\chi_r^2}$  Remains a Robust Measure of the Parameter Uncertainty<sup>a</sup>**

1 $\sigma(\chi)$ uncertainty	estimated 1 $\sigma$ uncertainty	$\chi_r^2$	$\sigma R_i$ (Å)	$\sigma R_i \sqrt{\chi_r^2}$ (Å)
0.20	1.0	0.0513	0.0185	0.00419
0.20	0.50	0.141	0.00937	0.00352
0.20	0.10	4.25	0.00188	0.00388
0.20	0.05	17.7	0.000944	0.00397
0.20	0.025	69.0	0.000453	0.00376

<sup>a</sup>Here, we model a single sine wave frequency with noise (Figure 6).

uncertainty and noise are estimated as equivalent with a  $\sigma(\chi) \simeq 0.2$  and  $\chi_r^2 \simeq 1$ .

Conversely, as the experimental data uncertainty improves (reduces, see Table 2), so long as the prediction of uncertainty

**Table 2. Simple Illustration Demonstrating that Collecting More Accurate Experimental Data Allows Parameters in the Model to Be Determined to Greater Precision<sup>a</sup>**

1 $\sigma$ uncertainty	$\chi_r^2$	$\sigma(R_i)$ (Å)
1.0	1.09	0.0218
0.50	1.24	0.00971
0.33	1.04	0.00583
0.20	1.19	0.00368
0.10	0.705	0.00183
0.05	1.21	0.000923
0.0025	0.911	0.000459

<sup>a</sup>We highlight the parameter  $R_p$ , as it applies to the discussion presented. Here, we model a single sine wave frequency with noise (Figure 6).

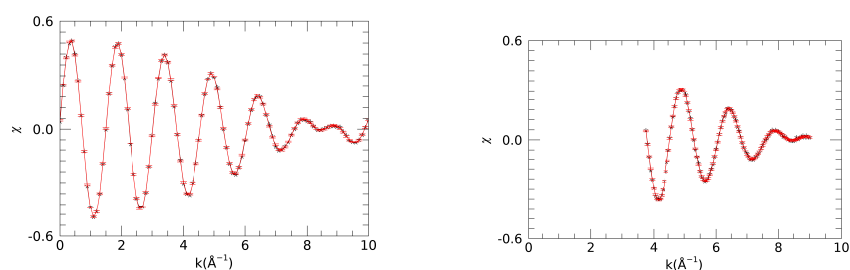
matches the data uncertainty, the uncertainty on a particular parameter, such as, especially, the fitted, determined shell radius, is given to higher and higher accuracy from  $2.00 \pm 0.02$  Å down to, for example,  $2.0000 \pm 0.0005$  Å. In other words, the data and the uncertainty in the data points are key and determine the accuracy of structural parameters. Collecting data with smaller uncertainties allows one to determine the

(XAFS) model parameters to greater precision. This should be fairly intuitive. Hence, a valid estimate of uncertainty allows statistical analysis to probe hypotheses of model, theory, structure, bond distances, and shells and other physically meaningful parameters. The idea that should be paramount is to let the data dictate the limit of hypothesis testing and insight. Now let us consider Nyquist-like prescriptions commonly discussed and used across the XAFS community. The Nyquist frequency is a well-defined minimum aliasing frequency from discrete signal processing; if the sampling or average sampling rate is  $\delta k$ , then one cannot determine components less than  $f_{\text{Nyquist}} = \frac{\delta k}{2}$ . In context, this means that it will not be possible to determine a Fourier transformed  $\Delta R$  radius of scatterer larger than, for example,  $\Delta R = \frac{\pi}{2f_{\text{Nyquist}}}$  where  $\frac{\pi}{2}$  indicates that the transform goes from peak to zero for destructive interference.

This prescription is commonly inverted to yield a minimum  $\delta R$  from a maximum  $k_{\text{max}}$  or preferably from a maximum  $\Delta k_{\text{range}}$  across which the data is sampled. The key argument then is that two components from two radial shells (of similar atomic number and scattering) will beat depending upon their phase and their combined amplitude will decrease with  $k$  until a minimum occurs. If one has sufficient data over a sufficient  $k$ -range, then one can determine the radial separation, the phase kink or offset, and the overall amplitude. From the requirement to reach or measure the minimum, we have the standard criterion<sup>5</sup>

$$\delta R = \frac{\pi}{2\Delta k} \quad (1)$$

Hence, if  $k_{\text{max}} = 15 \text{ \AA}^{-1}$  or  $\Delta k_{\text{range}} = 15 \text{ \AA}^{-1}$ , then  $\delta R \simeq 0.1 \text{ \AA}$ ; similarly, if  $\delta k_{\text{range}} = 7.5 \text{ \AA}^{-1}$ , then  $\delta R \simeq 0.2 \text{ \AA}$ . This has been presented regularly as a fundamental limit of XAFS analysis or other Fourier transform data collection. However, depending upon one's transform convention, or using the Rayleigh criterion, or using a more advanced theory to fit a fraction of a peak width, one can report a minimum as a factor of  $2\pi$  smaller or even less than this, as illustrated in Figures 6 and 7 and in Table 2. This equation or heuristic should be more like the minimal change that cannot be ignored rather than the minimal change that can be detected. Reference 5 correctly states that with arbitrarily good signal and noise, the resolution



(a) Two radii, noise,  $0 < k < 10$ , +typical thermal  $\sigma$  (b) With restricted  $3.75 < k < 9$

**Figure 7.** Fitting two nearby bond radii with noise to accuracies far below the Nyquist interpretation, so long as data points have high and known accuracy and uncertainties are maintained and propagated. Separate radii  $R_1 = 2.161 \text{ \AA}$ ,  $R_2 = 1.966 \text{ \AA}$  are estimated correctly to within one SE with an accuracy of  $0.001 \text{ \AA}$  (a) or even  $0.005 \text{ \AA}$  (b) for a short-ranged spectrum. Input noise and corresponding estimated uncertainty are  $\sigma(\chi) = 0.005$  and corresponding  $\chi_r^2 \simeq 1$ . The thermal broadening added with the estimated width does not significantly impact the structure nor the accuracy of the determination of parameters. Amplitudes are correctly fitted within one SE uncertainty of 0.4% (a) or 4% (b), and phases are correctly fitted to within one SE uncertainty of  $0.012^R$  (a) or  $0.08^R$  (b). Normal least-squares fitting is well able to correctly separate radial distances differing by, e.g.,  $0.195 \text{ \AA}$ .

of different distances can be increased; however, with correlation of parameters and noise, this could be more limited. Clearly, this limit can also be improved upon if the scatterers are different in type or degeneracy.<sup>31</sup> These variations are not “Nyquist” prescriptions since the data is sampled in  $k$ -space, so the minimum aliasing limit is also in  $k$ -space, not transformed space.

Thermal broadening damps the sine waves and increases with  $k$  and hence can be correlated with the beat from the two shells. This is included in (standard) correlated least-squares fitting analysis. In general, with good experimental data or well-defined uncertainties, these correlations can be overcome and separate closely spaced radial shell distances can be distinguished. We illustrate this in Figure 7. Here, we model two nearby frequency sine waves, closely matching our experimental data, with added Gaussian noise as in the earlier illustration. This mimics two bonding radii equivalent to the best fit of our experimental data model. With correctly defined uncertainties and noise, it is straightforward to determine separate radial distances below this Nyquist or aliasing limit. It is not in conflict with signal processing, but rather it is the consequence of signal processing. In the figure, even a short fitting range of  $k$  can identify separate nearby shell radii to high accuracy, some 100 times more accurate than the separation, so long as the data quality is sufficient. If the uncertainties or noise is too large or if parameters are not independent but are highly correlated, then the limit is weaker and the resolution of, for example, two shells is weaker. An understanding of non-Gaussian distributions and cumulants can also confirm this finding.

**Number of Independent Data Points.** Two measures of data quality or extent need to be clearly separated: the number of (independent) data points in an XAS measurement across the energy or  $k$ -range  $N$  or  $N_{\text{idp}}$  and the “effective number of independent parameters”  $N_{\text{ipar}}$ , which can be fitted (well) in a least-squares analysis. In a step-scan experiment where each measurement is made independent of the next, each data point is independent and the total in a fitting  $k$ -range is  $N$  or  $N_{\text{idp}}$ . The number of parameters actually fitted (not constrained) in a model is then  $N_{\text{par}}$ . There may be some particular systematic uncertainties in common, but the counting uncertainties and variances are independent. To get from raw  $\left[\frac{\mu}{\rho}\right]$ -versus- $E$  data to the  $\chi$ -versus- $k$  spectrum involves a variety of possible operations that can change the real or apparent number of independent points. In the first part of this discussion,<sup>7</sup> we have explained how to preserve the number of independent points and what this means. However, it is common to interpolate data and apply several background and spline subtractions, etc., and each process can change the correlations of adjacent points but not the original noise and variance. It is possible in a fast continuous scan to have the detector response function (not just the dead-time) too short for the experimental data to be truly independent. Hence, we strongly recommend considering the raw data statistic and variance and propagating this for the independent points, rather than making a uniform grid where correlations will locally ensue. For a review, see ref 12.

One can ask which data points are relevant or useful to determine the first shell radius and which of them contribute to a particular fitting parameter. For example, pre-edge data does not contribute to measuring the first shell bond length and only the data transformed into the  $\chi$ -versus- $k$  space contributes

to the shell radii or any other standard XAFS parameter determination. Equally, very high  $k > 25 \text{ \AA}^{-1}$  data does not normally contribute significantly to any XAFS fitting parameter. However, the data points (within a fitting window) remain independent unless, for example, they have been heavily interpolated. When interpolating to either a fine or finer  $\chi$ -versus- $k$  grid to, for example, 0.04 or 0.10  $\text{\AA}^{-1}$  or when transforming and interpolating to  $a$ , for example, 0.04  $\text{\AA}$  spacing  $\chi$ -versus- $R$  grid, one is adding no new independent data points and no additional information content on any parameter; indeed, one is usually removing information content.<sup>12</sup>

$N_{\text{idp}}$  is an alternate measure of “effective estimated number of independent points” in the XAFS spectra given by the Nyquist formula or, variously, the Nyquist theorem (but not following Nyquist)

$$N_{\text{idp}} = \frac{2\Delta k \Delta R}{\pi} \quad (2)$$

for a fit range of  $\Delta k$  and  $\Delta R$  in  $k$ - and  $R$ -space, respectively.<sup>5</sup> In practice,  $\Delta k$  is estimated or defined as the range of  $k$  being fitted (within some Hanning window, for example) or the range of  $k$  being used to create the transform of the experimental data into  $R$ -space. Similarly,  $\Delta R$  is estimated as the Fourier filtered or fitted range used in the transform into  $R$ -space. Alternatively,

$$N_{\text{idp}} = \frac{2\Delta k \Delta R}{\pi} + I \quad (3)$$

where  $I$  is claimed to be unity<sup>32</sup> or 2.<sup>33</sup>

The idea as presented is that this is the maximum number of independent parameters that can be fitted for this data set. Naturally, if two parameters are not independent but are 100% correlated, then one can only ever fit one or the other, and most XAFS parameters have significant correlation matrices with other parameters, so that this number can be seen as an overestimate. Refs 3 and 34 saw the need to replace  $N_{\text{idp}}$  with a more useful and relevant measure to define the effective size of the parameter space. Refs 26 and 35 concluded that the actual fitting space in such a transformed fitting is commonly significantly less than even the lower estimate above, which in one example appeared to correspond to  $I = -5$ .

If we define a fit range of  $\Delta k$  and an average spacing of data points across this range of  $\delta k$ , then it is clear that the number of independent data points should be  $N_{\text{idp}} = \frac{\Delta k}{\delta k}$ ; if we use the earlier prescription  $\Delta R < \frac{\pi}{2\delta k}$ , then we could have  $N_{\text{idp}} = \frac{2\Delta k \Delta R}{\pi}$  noting the limitations of this prescription from above, and one can see the etiology (and error) of the last equation.

Much data is fitted in  $k$ -space, whether using  $\chi$ ,  $k\chi$ , or  $k^2\chi$  as the fitted function. The theory is determined over all  $R$ -space and can be transformed into  $k$ -space. The theoretical determination can be limited to a number of paths and hence a range of radii; however, one can consider  $\Delta R \simeq \infty$ , implying from the formula that any number of parameters can be fitted up to the number of data points or the number of independent data points if extensive interpolation, correlation, or preprocessing is done. The number of parameters that can be fitted, and their uncertainty, depends upon the uncertainty of the data, their spacing, and their relevance to the parameters to be fitted.

In current usage, these estimates of the maximum number of independent parameters  $N_{\text{idp}}$  should be considered as empirical heuristics with the correct value, differing by a possible large factor, to be found from freeing the most significant near-independent parameters one by one until the correlation matrix and array of uncertainties prove that the data set is not able to reliably determine the next (independent) parameter. In other words, the covariance matrix should explicitly indicate the ability to fit each parameter with whatever the experimental and modeling correlations there may be, and it also gives strong indications when too many parameters are being fitted, so long as experimental uncertainties are used in the analysis. This is in agreement with the least-squares covariance matrix, the maximum entropy correlation matrix, and Bayesian approaches.

**Definition of  $\chi_r^2$ .** Rather than being used as a heuristic guideline of the maximum limit of parameters,  $N_{\text{idp}}$  is also commonly used in the definition of  $\chi_r^2$ ,<sup>5,33,36,37</sup> the  $\chi^2$  per degree of freedom

$$\chi_r^2 = \frac{\chi^2}{N_{\text{idp}} - N_{\text{par}}} \quad (4)$$

In our current example, we have  $N_{\text{idp}} \sim 122$  and  $N_{\text{par}} \sim 4$ . Conversely, an incorrect prescription that distorts hypothesis testing and relative model agreement is

$$\chi_r^2 = \frac{\chi^2}{N_{\text{indp}} - N_{\text{par}}} \quad (5)$$

where  $\Delta k \sim 6.25 \text{ \AA}$  and  $\Delta R$  might be  $2 \text{ \AA}$  so  $N_{\text{indp}}$  might be estimated as 9 (or 10, 11, or less, following the above alternatives) so that the denominator becomes ca. 5 and the  $\chi_r^2$  will be very high and also highly sensitive to adding parameters, leading some to recommend an additional scaling. However, the denominator should represent the data and the estimate of independent parameters should be given by the least-squares covariance matrix or equivalently the maximum entropy method. Some studies have shown that these types of (unknown) errors have meant that  $\chi_r^2$  is not useful in the normal sense<sup>38</sup> or that it should be normalized yielding only a relative local measure,<sup>39</sup> almost invalidating it for hypothesis testing.

Reference 33 stated the need for the denominator to be increased. In the example of lead metal fitting, ref 40 needed to increase  $N_{\text{idp}}$  by 2 relative to an earlier work to permit fitting of additional parameters, apparently successfully. Their study showed that it was important and necessary that the denominator allows more parameters without reaching the singularity—if the correct denominator had been used, this would not have been necessary. While ref 35 seems to correct the denominator error in the Results section, this has not been applied by others or major software packages. Meanwhile, ref 41 has pointed out the inadequacy of using  $N_{\text{idp}}$  as a measure or as a determinant of  $\chi_r^2$ , noting that it is at odds with standard statistical analysis. Among other details, the study notes the importance of the F-test.

At the heart of this is the need to define and propagate the individual data uncertainties so that appropriate measures of goodness-of-fit and hypothesis testing can be made.<sup>12</sup> The analysis herein uses data with defensible uncertainties propagated, though there is more work to be developed in this general field. In this analysis, as it should always be, the

denominator is the number of (independently measured) data points (e.g., ca. 122) minus the number of fitted parameters (e.g., ca. 4).

It is possible to make useful recommendations for the following: add fitting parameters as close to being independent as possible and avoid simultaneously fitting redundant or highly correlated parameters; constrain or define additional parameters a priori if possible; avoid interpolation and try to define and propagate original raw data uncertainty and variance; fit additional parameters until the correlation matrix and the uncertainties demonstrate that the information content is not adequate for additional fitting parameters; at all points, use the denominator for  $\chi_r^2$  as  $N_{\text{idp}} - N_{\text{par}}$ , not  $N_{\text{ipar}} - N_{\text{par}}$ ,  $N_{\text{indp}} - N_{\text{par}}$ , or some other measure.

## RESULTS

**Structural Investigation of Nickel Complexes.** The published analysis of the absorption data identified two possible geometries for the nickel complex materials. The two geometries are presented in Figure 8. The structural

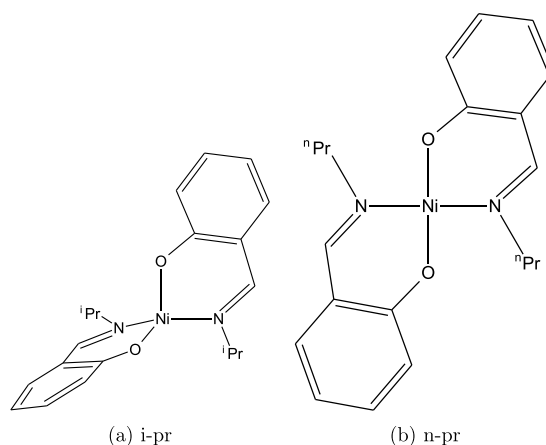


**Figure 8.** Structures of the limiting isometric forms of bis(*N*-propylsalicylaldiminato) nickel(II) where <sup>i</sup>Pr and <sup>n</sup>Pr represent *i*-propyl and *n*-propyl groups, respectively. These structures are referred to as (*i*-pr) and (*n*-pr) structures.

analysis used the multiple-scattering formalisms within FEFF8 following the IFEFFIT package<sup>42</sup> to generate theoretical XAS spectra for the two geometries considered. These theoretical models were then compared to the experimental data using the eFEFFIT package.<sup>12</sup> We investigate two 15 mM complexes with 0.1% w/w of the active Ni species. Similar observations are obtained for 1.5 mM or 100 ppm systems.

The absorption data is a single set, with well-defined experimental uncertainties, including detailed systematic effects quantified by XERT in transmission, and discussed in a preliminary form<sup>10</sup> and with careful discussion and propagation of uncertainty.<sup>12</sup> Here, we investigate the same structures but completely different data sets collected in fluorescence and therefore requiring new analysis to derive uncertainty estimates, correct for systematic effects, and propagate to the  $\chi$  versus  $k$  spectra prior to processing<sup>7</sup> and leading to the analysis herein. The fluorescence data is a set of 33 spectra, collected from each pixel in a square-planar detector.

One dramatic improvement should be mentioned here: the raw fluorescence spectra and any simple normalizing spectra

have increasing slopes above the edge or even no slope if they are “flattened” by software. The theoretical predictions scale the XAFS oscillations by the atomic or background (spline) denominator, which must follow a valid absorption shape and go down with energy above the edge. Hence, in general,  $S_0^2$  values and the relative amplitudes of oscillation can be skewed functions of  $k$  and increasingly distorted above the edge from 10 to 50% at higher  $k$  in the absence of the SeAFFluX correction. This is a potentially large systematic distortion and fully corrected for with SeAFFluX (see ref 7), so we do not propagate a large error but only propagate a modest uncertainty. Conventional fluorescence analysis does not propagate uncertainties, so even the simpler prescriptions have added value.

**Defining the Data and Structural Models.** We began with square-planar and tetrahedral structural models for these samples as reported in the literature and refined these to best fit our data. We fit a model for the first 75 or 71 paths, which covers all symmetries, common paths, and unique paths, out to a half-length of 4.85 Å and especially including, for example, the Ni–N–Ni–N–Ni or Ni–N–N–Ni and Ni–O–O–Ni paths at around 3.8 or 4.2 Å, which are favored in the linear arrangement (square-planar) compared with the tetrahedral arrangement. The most important parameters to be refined were, as in most XAFS analysis,  $S_0^2$ ,  $\alpha$ ,  $\Delta E_0$ , and  $\sigma^2$ . The next most important parameters to be refined were the Ni–N and Ni–O bond lengths and the N–Ni–O angle, since these are crucial in determining the difference between the two potential structural models. Unlike in crystal analysis, we have previously proven that there is only a single Ni–N distance and a single Ni–O bond length. We also added distinct  $\sigma^2$  parameters for the two-legged Ni–N–Ni and Ni–O–Ni paths and separately for the next shortest 15 photoelectron paths. Finally, we added two extra parameters to refine the Ni–C bond lengths as these are the next most important after the Ni–N and Ni–O bond lengths.

**$k$ -Window Selection.** The data was converted from  $a_i \left[ \frac{\mu}{\rho} \right]$  versus  $E$  to  $\chi$  versus  $k$  for structural analysis, preserving the uncertainty propagation, following mu2chi software.<sup>12</sup> Muffin-tin theoretical predictions are known to be of poor accuracy at low  $k$ , and an error in  $E_0$  or the spline is the most significant and manifests at low  $k$ , so it has been a well-defined understanding to have a low- $k$  cutoff for the Hanning window of, for example,  $k = 3.0$ .<sup>43</sup> This assumption or limit has been commented upon by Rehr<sup>42,44</sup> with latest versions of FEFF being, under some conditions, able to reach below  $k = 3$  to make a valid theoretical prediction. The development of FDMX without a muffin-tin assumption has demonstrated in a range of cases (especially where the energy scale is calibrated to minimize  $E_0$  errors) that theory can predict experimental data significantly below  $k = 3$  and even to  $k = 1$ .<sup>30</sup> With standard eFEFFIT fitting except for the uncertainties, the absorption data were initially fitted in a conservative  $k$ -range  $k \in [3.3, 9.0]$  Å<sup>-1</sup>, using  $\chi_r^2$ . This is defined for  $\alpha$  independent variables  $x_i$  with mean  $\mu_i$  and variance  $\sigma_i^2$  as

$$\chi_r^2 = \frac{\sum_{i=1}^{N_{\text{idp}}} \frac{(x_i - \mu_i)^2}{\sigma_i^2}}{N_{\text{idp}} - N_{\text{par}}} \quad (6)$$

where  $N_{\text{idp}}$  is, as earlier, the number of data points and  $N_{\text{par}}$  is the number of fitted parameters. Clearly, from the figures, the

uncertainties at low  $k$  ( $k < 3.8$ ) are particularly small and will unduly bias the fitting routine if fitting to ill-defined theory. This is well known in fitting to theory; many users would routinely use  $k_{\text{min}} \approx 3$  anyway. For uncertainties derived from the variance and consistency of the data, these data sets clearly demonstrate that the theory used is unable to fit well across the region [3.3, 3.75], which distorts the fits, the residuals, and the parametrization. This is evident in Figure 9. When fitting over

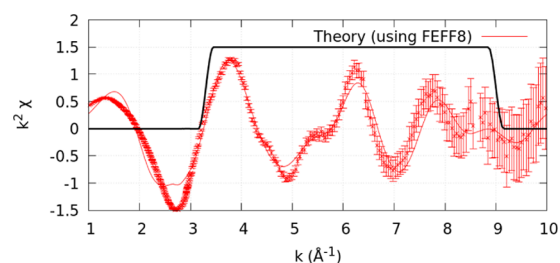


**Figure 9.**  $k$ -Range: result of fitting with a  $k$ -window  $k \in [3.3, 9.0]$  Å<sup>-1</sup> with too low a  $k_{\text{min}}$ . The small uncertainties in the low- $k$  region bias the fitting routine toward the less-well-defined theory and favor the first peak within the fitting region, at the expense of subsequent peaks.

a region beginning too low in  $k$ , a much higher  $\chi_r^2$  is returned (Table 3: 2.2 and 5.2, respectively, for  $i$ -pr and  $n$ -pr for the

**Table 3. Results of Fitting Fluorescence Data over the  $k$ -Range [3.3, 9.0] with Too Low a  $k_{\text{min}}$ <sup>a</sup>**

model geometry	tetrahedral	square-planar
Ni–N (Å)	2.161 ± 0.012	2.109 ± 0.013
Ni–O (Å)	1.966 ± 0.006	1.909 ± 0.007
N–Ni–O (deg)	93.63 ± 1.23	89.40 ± 1.23
Ni–C <sub>1</sub> (Å)	2.856 ± 0.012	2.758 ± 0.019
Ni–C <sub>2</sub> (Å)	3.018 ± 0.012	2.933 ± 0.016
$N_{\text{idp}}$ in fit range	138	138
	<b><math>i</math>-pr data</b>	<b><math>n</math>-pr data</b>
$\chi_r^2$	<b>2.22</b>	<b>5.16</b>
$S_0^2$	1.413 ± 0.061	1.141 ± 0.053
$\alpha$	0.987 ± 0.003	0.976 ± 0.006
$\sigma_{\text{N}}^2, \sigma_{\text{O}}^2$ (Å <sup>2</sup> ) <sup>b</sup>	0.001 <sup>c</sup>	0.001 <sup>c</sup>
$\sigma_{\text{short}}^2$ (Å <sup>2</sup> )	0.002 <sup>c</sup>	0.002 <sup>c</sup>
$\sigma^2$ (Å <sup>2</sup> )	0.010 ± 0.001	0.025 ± 0.003
$E_0$ (eV)	3.349 ± 0.714	0.017 ± 0.842

<sup>a</sup>Bold font indicates the correct solution for the structure in the table. <sup>b</sup> $\sigma_{\text{N}}^2$  and  $\sigma_{\text{O}}^2$  are for the two-legged Ni–N–Ni and Ni–O–Ni paths, set to 0.001 Å<sup>2</sup>. <sup>c</sup>Fixed to a physical value.  $\alpha$  is the bond and path-scaling parameter for all paths except for the innermost four paths grid-searched in the table.

lower  $k_{\text{min}} = 3.3$  versus 1.3 and 1.6 for  $k_{\text{min}} = 3.75$ ). More worryingly, the optimized structural models are markedly different to the models optimized by fitting over the  $k$ -range [3.75, 9.0]. In investigations of samples with subtly different molecular structures, such errors easily lead to misleading conclusions. Therefore, in this analysis, we fit over  $k \in [3.75, 9.0]$  Å<sup>-1</sup>. Significant structural information is not lost by this choice of fitting window, since the number of points within the fitting region is only changed from  $N_{\text{idp}} = 138$  to  $N_{\text{idp}} = 121$  ( $i$ -pr) and from  $N_{\text{idp}} = 136$  to  $N_{\text{idp}} = 122$  ( $n$ -pr).

Figure 5 illustrates the remarkable consistency of the  $\chi$  functional from both transmission and fluorescence and the consistency of the uncertainty magnitude and functional across

the  $k$ -range. This proves very strongly that at least for 15 mM solutions, or 0.1% w/w active species, both transmission and fluorescence are excellent and competitive, with suitable analysis.

**Nanostructure.** Despite this great success of the analysis and uncertainties for fluorescence, the spectra of  $i$ -pr and  $n$ -pr Ni complexes look identical (Figure 10). Are the structures

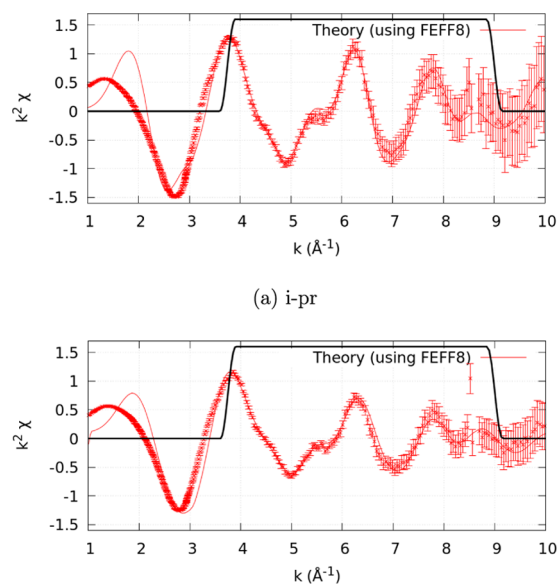


**Figure 10.** Final data and excellent fitted theoretical models with adjusted  $k$ -window of  $k \in [3.75, 9.0] \text{ \AA}^{-1}$ . We highlight the two peaks in the XAFS at  $k \approx 4.4$  and  $5.4 \text{ \AA}^{-1}$ , respectively, not recognized and not fitted in the past analyses.

distinguishable, and what distinct parameters can be determined from the data? Figure 10 reveals discrete and significant differences between the two data sets, corresponding to different structures. The  $k$ -range seems narrow compared with a number of standard XAS (IFEFFIT) fits from high-flux beamlines; one might expect good-quality data out to  $k \sim 12$  or more. While this analysis has concentrated on proving the limitation of theory, perhaps surprisingly, in the range  $k_{\min} \in [3.3, 3.75] \text{ \AA}^{-1}$ , the high- $k$  region ( $k > 9 \text{ \AA}^{-1}$ ) looks good and could be incorporated in the fits. However, the information content, given by the uncertainties, does not grow uniformly or linearly. The uncertainties give a natural cutoff for the upper limit  $k_{\max}$  of around 9, 10, or 11, quite different from standard treatments but without loss of generality or loss of information. If this were a problem, linking to the discussion of the number of independent parameters and the definition of  $\chi_r^2$ , then it would limit the number of independently determinable parameters; however, it has very little effect on parameter evaluation.

We observe two peaks in the XAFS at  $k \approx 4.4$  and  $5.4 \text{ \AA}^{-1}$ , not significant in past analyses. The two peaks appeared in the transmission spectra, but the significance there was marginal and the features were not recognized nor fitted by the standard (modified) fitting program. The peaks are clear and significant in the fluorescence spectra of both nickel(II) complexes and need to be fitted to obtain good  $\chi_r^2$ . While these have not been fitted before, they are indeed fitted well, as seen in Figure 10, for both structures. This improved fitting and structure suggest that the uncertainties presented may be slightly overestimated and that the fitted models appear to match well beyond the

fitting range, to above  $k \sim 10 \text{ \AA}^{-1}$ . Even in this high- $k$  range, the discrepancies are not normally distributed noise but are dominated by systematic local deviations in structure. Thus, a key result of correcting for self-absorption and of error propagation is the identification and fitting of new structural information. Multielectron excitations (shake processes and the amplitude reduction factor  $S_0^2$ ) are important theoretically, and we note that the transform to  $k$ -space can add to or amplify uncertainty and error correlated with this parameter. It should remain less than or equal to unity, within three standard errors.

The  $i$ -pr Ni complex (Figure 10a) is found to be tetrahedral (distorted), and the  $n$ -pr Ni complex is found to be distorted square-planar, that is, rhombohedral (Figure 10b). Tables 4

**Table 4.**  $i$ -pr Structure is Tetrahedral<sup>a,b</sup>

model geometry	tetrahedral	square-planar
Ni–N (Å) <sup>c</sup>	1.999 ± 0.005	2.045 ± 0.056
Ni–O (Å) <sup>c</sup>	2.060 ± 0.006	2.022 ± 0.042
N–Ni–O (deg)	89.54 ± 1.23	92.31 ± 1.23
Ni–C <sub>1</sub> (Å)	2.937 ± 0.023	2.898 ± 0.012
Ni–C <sub>2</sub> (Å)	2.943 <sup>d</sup>	2.943 <sup>d</sup>
<b><math>i</math>-pr <math>\chi_r^2</math></b>	<b>1.285</b>	2.369
$\Delta E_0$ (eV)	2.98 ± 0.51	4.00 <sup>d</sup>
$S_0^2$	1.00 ± 0.05 <sup>d</sup>	0.85 ± 0.05 <sup>d</sup>
$\alpha$	1.002 ± 0.002	1.001 ± 0.003
$\sigma_{\text{Ni}}^2, \sigma_{\text{O}}^2$ (Å <sup>2</sup> ) <sup>c</sup>	0.001 <sup>d</sup>	0.001 <sup>d</sup>
$\sigma_{\text{short}}^2$ (Å <sup>2</sup> ) <sup>f</sup>	0.002 <sup>d</sup>	0.002 <sup>d</sup>
$\sigma^2$ (Å <sup>2</sup> )	0.003 ± 0.001	0.009 ± 0.002

<sup>a</sup>Refined positions and bond distances for both models using  $k \in [3.75, 9.0] \text{ \AA}^{-1}$ . An excellent agreement is found between the results presented here and the results previously published using transmission data. This is a powerful statement on the quality and accuracy of the data and analysis possible from fluorescence. <sup>b</sup>Bold font indicates the correct solution for the structure in the table. <sup>c</sup> $\sigma_{\text{Ni}}^2$  and  $\sigma_{\text{O}}^2$  represent the two-legged Ni–N–Ni and Ni–O–Ni paths, set to 0.001 Å<sup>2</sup>. <sup>d</sup>Fixed to a physical value.  $\alpha$  is the bond and path-scaling parameter for all paths except for the innermost four paths grid-searched in the table. <sup>e</sup>As always with XAS, the identification of N or O as the nearest neighbor is not well determined; see the text <sup>f</sup> $\sigma_{\text{short}}^2$  is the thermal broadening parameter for the next shortest 15 photoelectron scattering FEFF paths, set to 0.002 Å<sup>2</sup>.  $\sigma^2$  is the free parameter for all farther paths.

and 5 present the optimal  $\chi_r^2$  solutions of the two structures contrasted with the unphysical counter-hypotheses. Clearly, the wrong assignments find distorted positions and significantly higher  $\chi_r^2$  of 2.4 and 1.7 instead of the preferred models  $\chi_r^2$  of 1.29 and 1.59, indicating that there is strong evidence for local geometry in the data, even between models with no change in the number of coordinated atoms (4 for both tetrahedral and square-planar). We note that a  $\delta\chi_r^2 \sim 0.12$  is a small change and one can question the significance; in context, this has the same number of parameters in both cases with the same constraints and the  $\Delta\chi^2 \sim 14$  implies the significance according to the  $F$ -test. Higher-order paths differentiate between these models, and the data and uncertainty are good enough to distinguish them. At this level, this is consistent with transmission data.<sup>11,12</sup>

## DISCUSSION

Theory and experimental spectra are not consistent or comparable below  $k \sim 3.75$ . The discrepancy is not due to

Table 5. *n*-pr Structure Appears to Be Square-Planar<sup>a,b</sup>

model geometry	tetrahedral	square-planar
Ni–N (Å) <sup>c</sup>	1.952 ± 0.002	2.123 ± 0.002
Ni–O (Å) <sup>c</sup>	2.063 ± 0.002	1.939 ± 0.001
N–Ni–O (deg)	90.40 ± 1.23	89.36 ± 1.23
Ni–C <sub>1</sub> (Å)	2.863 ± 0.008	2.858 ± 0.008
Ni–C <sub>2</sub> (Å)	2.969 ± 0.004	2.954 ± 0.004
<b><i>n</i>-pr <math>\chi_r^2</math></b>	1.702	<b>1.588</b>
$\chi^2$	197	<b>183</b>
$\Delta E_0$ (eV)	4.00 <sup>d</sup>	4.00 <sup>d</sup>
$S_0^2$	0.90 ± 0.05 <sup>d</sup>	1.00 ± 0.05 <sup>d</sup>
$\alpha$	0.997 ± 0.001	1.002 ± 0.001
$\sigma_{\text{Ni}}^2, \sigma_{\text{O}}^2$ (Å <sup>2</sup> ) <sup>c</sup>	0.001 <sup>d</sup>	0.001 <sup>d</sup>
$\sigma_{\text{short}}^2$ (Å <sup>2</sup> ) <sup>f</sup>	0.002 <sup>d</sup>	0.002 <sup>d</sup>
$\sigma^2$ (Å <sup>2</sup> )	0.003 ± 0.001	0.012 ± 0.001

<sup>a</sup>Refined positions and bond distances for both models using  $k \in [3.75, 9.0] \text{ \AA}^{-1}$ . An excellent agreement is found between the results presented here and the results previously published using the absorption data. This is a powerful statement on the quality and accuracy of the data and analysis possible from fluorescence XAS. <sup>b</sup>Bold font indicates the correct solution for the structure in the table. <sup>c</sup> $\sigma_{\text{Ni}}^2$  and  $\sigma_{\text{O}}^2$  represent the two-legged Ni–N–Ni and Ni–O–Ni paths, set to 0.001 Å<sup>2</sup>. <sup>d</sup>Fixed to a physical value.  $\alpha$  is the bond and path-scaling parameter for all paths except for the innermost 4 paths grid-searched in the table. <sup>e</sup>As always with XAS, the identification of N or O as the nearest neighbor is not well determined; see the text. <sup>f</sup> $\sigma_{\text{short}}^2$  is the thermal broadening parameter for the next shortest 15 photoelectron scattering FEFF paths, set to 0.002 Å<sup>2</sup>.  $\sigma^2$  is the free parameter for all farther paths.

the data reduction, as the spline and  $E_0$  errors decrease with increasing  $k$ . Readers might be very comfortable with a lower  $k$  cutoff, as were we, but the accuracy of the low- $k$  data points makes the discrepancies of theory in this region striking. At the level of the uncertainties, the amplitude of oscillation in the experimental fluorescence spectra across this  $k$ -range is not reliably predicted by the FEFF8 theory. The  $\chi_r^2$  values are much more sensitive to the local structure, in part due to the small data point uncertainties. This allows us to define a lower  $k$  limit without an arbitrary assumption, based on the evidence of the data. Investigation can highlight where difficulties of any model arise and compare model or theory dependencies. This is very powerful as a tool of analysis.

We compare results presented using dramatically different fitting  $k$ -ranges, exposing a limitation of the theoretical model at, for example, low  $k$ . However, when the wider  $k$ -range is not robust, due to the limitations of theoretical modeling, it is not particularly useful to compare parameters and parameter uncertainties; it is demonstrated to be inadequate, for example, the use of a wider  $k$ -range. Raising the maximum  $k$ -value for fitting should be robust in that the uncertainties should define the significance of any high- $k$  range. However, the lower limit  $k_{\text{min}}$  will vary according to the theory used, not directly the structure modeled, and errors or discrepancies of  $r$  or  $\sigma^2$  may be directly introduced by fitting to a model below its range of validity.

A recent reanalysis of transmission data following ref 12 using a  $k$ -range  $k \in [3.75, 9.0]$ , as used here, yields results in good agreement with these current results compared to the original publication, which used a low  $k_{\text{min}}$ . Major improvements are made to the interpreted  $S_0^2$ , and significant changes occur to the bond lengths of inner-shell atoms upon reduction of the  $k$ -range to yield a better model fit for both transmission

and fluorescence data sets. Future work can investigate the structural problems with theory at low  $k$ , given that we can present highly accurate data with  $k$ -dependent uncertainties across this region.

After correction for self-absorption, the key nanostructural analysis results of the nickel complex spectra are presented in Tables 4 and 5. Here, there are 121 (*i*-pr) or 122 (*n*-pr) independent data points in the fitting region and four free-fitted parameters ( $\Delta E_0$ ,  $S_0^2$ ,  $\alpha$ , and  $\sigma^2$ ). An extensive grid-search investigated the detailed  $\chi_r^2$  valley shape and extent across the variables  $r_{\text{Ni-N}}$  and  $r_{\text{Ni-O}}$ , the dihedral internal angle N–Ni–O, the two closest carbon atoms Ni–C<sub>1</sub> and Ni–C<sub>2</sub>, and the unfortunate parameter  $S_0^2$ . The  $\chi_r^2$  valley is correlated with real uncertainty as to whether the N or the O is the closest to the active site (Ni) (see the Supporting Information). This is because the  $\chi_r^2$  valley has a double minimum so that the fitting procedure cannot easily distinguish the amplitude for N scattering compared with the amplitude for O scattering to determine the order of shells. Perhaps more importantly, the two innermost shells are clearly separated. Uncertainties in these grid-search parameters are determined from the corresponding one standard error uncertainties of the bond scaling parameter  $\alpha$ , resulting in the corresponding increase in  $\chi^2$ . Thermal parameters for the innermost shell  $\sigma_{\text{O}}^2$ ,  $\sigma_{\text{Ni}}^2$  are set to 0.001 Å<sup>2</sup>, while the next-nearest bonds are set to double this value. Then, the free-fitted parameter  $\sigma^2$  is for all farther paths, and is broadly consistent and physical. The individual shell thermal parameters have too little information to fit directly, but we expect significant differences between the inner shell and the outer paths, as observed. While there are small uncertainties in these fixed parameters, they are physically reasonable.

An excellent agreement is found between the predictions of our fluorescence spectra and the theoretical spectra given by the molecular structural models presented here.  $\chi_r^2$  values approach 1, indicating an excellent goodness-of-fit, further supported by Figure 10. The structures are distinct, and the cross-fitting of the models demonstrates a much higher  $\chi_r^2$  when the data is fitted by the model with the incorrect geometry.

**Earlier Investigations.** A major development is that we can now observe two major and significant features, peaks in the spectra, which could not be seen as significant in earlier (transmission) data sets nor in earlier analysis. These qualitative features allow us to conduct a more critical analysis and fitting for model and structural hypotheses.

Crystals of these molecules have been reported by room-temperature X-ray diffraction (RT XRD).<sup>8,9</sup> Our dilute solution experimental data at ca. 80 K has much lower thermal parameters, so the reported  $\sigma^2$  data from RT XRD are not relevant. Packing forces of the space group likely cause distortions in the regular molecule so that regularization of XRD structures is necessary for solutions. Although the temperature is reduced, the experimental data indicate that the molecular bonds are expanded in solution compared with the crystals, as expected by a comparison of the densities. Hence, the bond lengths of these structures are longer than those from X-ray diffraction, by about 0.07–0.08 Å or 4%. A rotated structure based on ref<sup>8</sup> serves as a much better fit to the experimental data for *n*-pr than the structure of ref,<sup>9</sup> even with optimization, likely due to the poor XRD determination. Conclusions of QuickXAFS data sets are consistent with Hybrid transmission XAFS. Similarly, the X-ray diffraction

found  $N_1$  and  $N_2$  to be inequivalent with bond lengths differing by 0.04 Å from the Ni, which is possible in a crystal structure but highly implausible in a dilute solution, necessitating regularization of equivalent bond distances.<sup>11</sup> In Table S2, we represent the structures of the crystallographic data and regularized past XAFS structural studies. The two room-temperature XRD structures are not expected to be identical to the corresponding solution structures, quite apart from the disorder, the theoretical difference between the mean-square lattice position and the mean-square bond length, and the structure of the environment. Islam et al.<sup>11</sup> carried out a structural determination from transmission data including Hybrid and QuickXAFS data sets, were unable to propagate nonuniform data spacing and direct experimental uncertainties in the fit, and were not able to make an extensive grid-search. By incorporating nonuniform data spacing, direct experimental uncertainties, and a three-dimensional grid-search, Schalken et al.<sup>12</sup> significantly improved the transmission analysis technique and the robustness of the analysis. The  $\chi_r^2$  values are defined by the new data uncertainties and so are not directly compatible. In these refinements, the “tetrahedral” structure is always best fit by a distorted tetrahedral structure and the “square-planar” structure is always best fit by a distorted square-planar structure. However, as discussed above, these advanced fits had larger uncertainties and omitted the two new features, in part because the  $k$ -range went beyond the valid theoretical lower limits, as explained earlier and analogously with Table 3. Hence, some distortion introduced in the fitted parameters because of this, which is clarified and resolved by the current analysis. In particular, this improved the stability and value of  $S_0^2$ , much improved the  $\chi_r^2$ , led to a more stable N–Ni–O angle accurate to about 1.2°, and led to shifts of bond distances by 0.01–0.04 Å or up to five standard errors.

Structural information can be extracted from fluorescence spectra of at least the same quality as transmission data, and both methods are fully valid for 15 mM solutions or 0.1% w/w samples. This can apply to samples not well-suited to transmission experiments. Data with uncertainties can reliably distinguish two shells closely spaced below the so-called Nyquist (or “aliasing”) limit, given careful analysis. The results presented here are far from the limit of what can be achieved with this modeling and data reduction. Figure 3 demonstrates how significantly greater accuracy and insight can be achieved by measuring relevant experimental thicknesses and distances to greater precision. Another development presented here compared to previously published transmission results is the optimization of the Ni–C bond distances. This is reflective of a more detailed structural analysis.

Some results in Tables 4 and 5 were restrained to take a physical value, indicative of the limits of fitting many correlated parameters simultaneously, even with good data. This need is dictated by the data, uncertainties, theory, fitting, and correlations. In general,  $S_0^2$  should not be above unity. This is correlated with  $\Delta E_0$ ,  $\alpha$ ,  $\sigma^2$ , and the  $k$ -range. Hence, a small error in  $\Delta E_0$  or from flattening of the extraction of  $\chi$  from  $\left[\frac{\mu}{\rho}\right]$ , which is a linear scaling error, will yield a slightly higher or lower value of  $S_0^2$ . This can be investigated further. The minimum  $\chi_r^2$  found, 1.17, related to Ni–N and Ni–O bond lengths is almost identical to these, with a slightly better separation of the two carbon distances and a similar  $\Delta E_0$ , but with  $S_0^2 = 1.16(6)$ , which is within three standard errors of unity. The bite angle should, from the literature and XRD

studies, be greater than 90°, and indeed the grid-search result lies within one standard error of this range.

The results of our structural analysis fitting found two minima with almost the same goodness-of-fit, corresponding to the interchange of Ni–N and Ni–O bond distances. In general, one would expect the Ni–O bond distance to be the shorter of the two, given the greater electronegativity of oxygen and as per the previous determinations of the X-ray diffraction crystal structures. However, it is very difficult to distinguish between similar distances and scatterers such as in the two models with the theoretical spectra used in this analysis. The model with the double-valley swapped (i.e., with the Ni–O bond being shorter) has almost the same  $\chi_r^2$  (1.33), residuals, and quality of fit, and of course, the electron densities are very similar (Table 6, Figure S1, Table S1). Most other parameter

**Table 6. Refined Bond Distances and Results for the *i*-pr Ni Data Set with the Model Where the Ni–N Bond Distance is Constrained to be Larger than the Ni–O Bond Distance<sup>a,b</sup>**

model geometry	tetrahedral
Ni–N (Å)	2.118 ± 0.009
Ni–O (Å)	1.937 ± 0.007
N–Ni–O (deg)	90.00 ± 1.225
Ni–C <sub>1</sub> (Å)	2.892 ± 0.026
Ni–C <sub>2</sub> (Å)	2.956 ± 0.012
$N_{\text{pts}}$ in fit range	121
<b><i>i</i>-pr <math>\chi_r^2</math></b>	<b>1.33</b>
$\Delta E_0$ (eV)	2.071 ± 0.675
$S_0^2$	1.189 ± 0.063
$\alpha$	0.996 ± 0.003
$\sigma_{\text{Ni}}^2, \sigma_{\text{O}}^2$ (Å <sup>2</sup> ) <sup>c</sup>	0.001 <sup>d</sup>
$\sigma_{\text{short}}^2$ (Å <sup>2</sup> ) <sup>e</sup>	0.002 <sup>d</sup>
$\sigma^2$ (Å <sup>2</sup> )	0.0062 ± 0.0012

<sup>a</sup>This model is not ruled out by the data and analysis. <sup>b</sup>Bold font indicates the correct solution for the structure in the table. <sup>c</sup> $\sigma_{\text{N}}^2$  and  $\sigma_{\text{O}}^2$  represent the two-legged Ni–N–Ni and Ni–O–Ni paths, set to 0.001 Å<sup>2</sup>. <sup>d</sup>Fixed to a physical value.  $\alpha$  is the bond and path-scaling parameter for all paths except for the innermost 4 paths grid-searched in the table. <sup>e</sup> $\sigma_{\text{short}}^2$  is the thermal broadening parameter for the next shortest 15 photoelectron scattering FEFF paths, set to 0.002 Å<sup>2</sup>.  $\sigma^2$  is the free parameter for all farther paths.

values remain consistent with this alternate identification of N and O locations. Hence, this more chemically sensible model cannot be ruled out by the data and analysis. Further work and perhaps an alternate theory are required.

Some may feel that  $\sigma_{\text{Ni-X}}^2 = 0.001 \text{ \AA}^2$  is a tiny value for the X=N and X=O paths, too small for zero point motion for Ni oxide, and would note an estimated value of  $\sigma_{\text{Ni-O}}^2 \sim 0.005 \text{ \AA}^2$  at 300 K. There is real uncertainty here, but it is well understood and normal that  $\sigma^2$  increases generally with the radius of the shell, where the larger shells are fitted well to approximately 0.005 Å (or even larger: 0.013 Å; see other fits). This investigation is conducted at low temperature (80 K), so the thermal motion is much reduced from 0.005 Å. It is theoretically possible that these inner shells have a low value of  $\sigma^2$ , yet the physical parameters are correctly ordered for thermal and radial parameters and likely within a factor of two for the fixed thermal parameters.

The separation of the two inner shells  $R_1 = R_{\text{Ni-N}}$  and  $R_2 = R_{\text{Ni-O}}$  in Tables 4 and 5 might seem problematic. Indeed, ref<sup>45</sup> notes  $\sigma_{\text{effective}}^2 = \frac{1}{2} \left( \sigma_{\text{Ni-O}}^2 + \sigma_{\text{Ni-N}}^2 + \left( \frac{R_2 - R_1}{2} \right)^2 \right)$  and hence the

separation of radii  $R_2 - R_1$  could perhaps be significantly less than 0.09 Å, with a fixed  $\sigma_{\text{Ni-X}}^2 = 0.001 \text{ \AA}^{-2}$ ; instead, the data could be consistent with, for example,  $R_2 - R_1 \sim 0.05 \text{ \AA}$  with  $\sigma_{\text{Ni-X}}^2 = 0.0025 \text{ \AA}^{-2}$ , or they could be consistent with a single shell radius with separation  $R_2 - R_1 = 0.00 \text{ \AA}$  with  $\sigma_{\text{Ni-X}}^2 \sim 0.005 \text{ \AA}^{-2}$ . This is a valid rough guideline for poorly resolved peaks and small radial separations. The last of these choices would be problematic in that the thermal parameters would no longer be correctly ordered.

We extensively investigated this parameter space and the radial distributions of the two inner shells. The freeing of the inner shell  $\sigma_{\text{Ni-X}}^2$  or the fixing of thermal parameters to a larger value failed to reduce the radial separation significantly yet was strongly contraindicated by the rapid increase of  $\chi_r^2$  by  $\sim 25\%$ .

## CONCLUSIONS

The demonstrated success of self-absorption and attenuation corrections allows deeper analysis and greater insight in structural determination. We observe new qualitative features—new significant peaks in the spectra not previously observed—which are significant structural features and must be fitted. We present and propagate experimental data uncertainties through to analysis and model the spectra in two very similar structures well and accordingly down to a  $\chi_r^2$  of order unity. The structures of the two data sets are well modeled by FEFF in the higher- $k$  region, but there are discrepancies even at  $k \sim 3.3$ , as revealed by the data accuracy. This approach and theory can be easily valid for systems up to 1.5 mM or 100 ppm of the active absorber, but much more can be expected with refinement of the approach. We clearly discriminate between the two data sets with distorted tetrahedral and distorted square-planar coordination geometries, despite both coordinations being 4-fold. We clearly identify separate shell radii as a consequence of the propagated uncertainties and models for the inner shell, well below the unperturbed Nyquist limits. We demonstrate the value of correctly ordered thermal parameters in these systems, and the hypothesis of a single unresolved shell with distortion of the thermal parameters is quite implausible. Hence, the added insight of uncertainty propagation and SeAFFluX permits separations of several complex and subtle hypotheses for structural and dynamic determination from XAFS. Some ambiguities of XAFS must remain, relating to the identification of nearby shells of almost identical electron density such as the N and O inner shells; resolving this will require careful data collection and error analysis. Further work will explore this challenge in greater detail.

## ASSOCIATED CONTENT

### Supporting Information

The Supporting Information is available free of charge at <https://pubs.acs.org/doi/10.1021/acs.jpca.9b10619>.

Discussion of a possible model where the Ni–N bond distance is constrained to be larger than the Ni–O bond distance; Figure S1 and Table S1, results of such a model; Table S2, summary of the literature of nearest neighbor bond distances and angles for both *i*-pr and *n*-pr complexes; Table S3, definitions of the symbols used throughout this article (PDF)

## AUTHOR INFORMATION

### Corresponding Author

Christopher T. Chantler – School of Physics, University of Melbourne, Parkville, VIC 3010, Australia; [orcid.org/0000-0001-6608-0048](https://orcid.org/0000-0001-6608-0048); Email: [chantler@unimelb.edu.au](mailto:chantler@unimelb.edu.au)

### Authors

Ryan M. Trevorah – School of Physics, University of Melbourne, Parkville, VIC 3010, Australia

Martin J. Schalken – School of Physics, University of Melbourne, Parkville, VIC 3010, Australia

Complete contact information is available at:

<https://pubs.acs.org/10.1021/acs.jpca.9b10619>

### Notes

The authors declare no competing financial interest.

## ACKNOWLEDGMENTS

The authors acknowledge S. P. Best and M. T. Islam for their experimental contributions to this work. They acknowledge the Australian National Beamline Facility.

## REFERENCES

- (1) Creagh, D. C.; Hubbell, J. H. Problems associated with the measurement of X-ray attenuation coefficients. I. Silicon. Report of the International Union of Crystallography X-ray Attenuation Project. *Acta Crystallogr., Sect. A: Found. Crystallogr.* **1987**, *43*, 102–112.
- (2) Creagh, D. C.; Hubbell, J. H. Problems associated with the measurement of X-ray attenuation coefficients. II. Carbon. Report on the International Union of Crystallography X-ray Attenuation Project. *Acta Crystallogr., Sect. A: Found. Crystallogr.* **1990**, *46*, 402–408.
- (3) Krappe, H. J.; Rossner, H. H. Error Analysis of EXAFS Measurements. *J. Synchrotron Radiat.* **1999**, *6*, 302–303.
- (4) Jaklevic, J.; Kirby, J.; Klein, M.; Robertson, A.; et al. Fluorescence Detection of EXAFS: Sensitivity Enhancement for Dilute Species and Thin Films. *Solid State Commun.* **1977**, *23*, 679–682.
- (5) Lee, Pa.; Citrin, P. H.; Eisenberger, P.; Kincaid, B. M. Extended X-ray Absorption Fine Structure - its Strengths and Limitations as a Structural Tool. *Rev. Mod. Phys.* **1981**, *53*, 769–806.
- (6) Newville, M.; Boyanov, B. I.; Sayers, D. E. Estimation of Uncertainties in XAFS Data. *J. Synchrotron Radiat.* **1999**, *6*, 264–265.
- (7) Trevorah, R. M.; Chantler, C. T.; Schalken, M. J.; et al. Solving Self-Absorption in Fluorescence. *IUCr* **2019**, *6*, 586–602.
- (8) Fox, M. R.; Orioli, P. L.; Lingafelter, E. C.; Sacconi, L. The Crystal Structure of bis-(N-isopropylsalicylaldiminato) nickel(II). *Acta Crystallogr.* **1964**, *17*, 1159–1166.
- (9) Britton, D.; Pignolet, L. H. Bis(N-*n*-propylsalicylideneaminato)-nickel(II). *Acta Crystallogr., Sect. C: Cryst. Struct. Commun.* **1989**, *45*, 819–821.
- (10) Chantler, C. T.; Islam, M. T.; Best, S. P.; Tantau, L. J.; Tran, C. Q.; Cheah, M. H.; Payne, A. T. High-accuracy X-ray Absorption Spectra from mM Solutions of Nickel(II) Complexes with Multiple Solutions Using Transmission XAS. *J. Synchrotron Radiat.* **2015**, *22*, 1008–1021.
- (11) Islam, M. T.; Chantler, C. T.; Cheah, M. H.; Tantau, L. J.; Tran, C. Q.; Best, S. P. Structural Investigation of mM Ni(II) Complex Isomers Using Transmission XAFS: the Significance of Model Development. *J. Synchrotron Radiat.* **2015**, *22*, 1475–1491.
- (12) Schalken, M. J.; Chantler, C. T. Propagation of Uncertainty in Experiment: Structures of Ni(II) Coordination Complexes. *J. Synchrotron Radiat.* **2018**, *25*, 920–934.
- (13) Best, S. P.; Wang, F.; Islam, M. T.; Islam, S.; Appadoo, D.; Trevorah, R. M.; Chantler, C. T. Reinterpretation of Dynamic Vibrational Spectroscopy to Determine the Molecular Structure and Dynamics of Ferrocene. *Chem. - Eur. J.* **2016**, *22*, 18019–18026.

- (14) Islam, M. T.; Trevorah, R. M.; Appadoo, D. R.; Best, S. P.; Chantler, C. T. Methods and Methodology for FTIR Spectral Correction of Channel Spectra and Uncertainty, Applied to Ferrocene. *Spectrochim. Acta, Part A* **2017**, *177*, 86–92.
- (15) Chantler, C. T.; Tran, C. Q.; Paterson, D.; Cookson, D.; Barnea, Z. X-ray Extended-Range Technique for Precision Measurement of the X-ray Mass Attenuation Coefficient and Im(f) for Copper Using Synchrotron Radiation. *Phys. Lett. A* **2001**, *286*, 338–346.
- (16) Chantler, C. T.; Tran, C. Q.; Paterson, D.; Barnea, Z.; Cookson, D. J. Monitoring Fluctuations at a Synchrotron Beamline Using Matched Ion Chambers: 1. Modelling, Data Collection, and Deduction of Simple Measures of Association. *X-Ray Spectrom.* **2000**, *29*, 449–458.
- (17) Chantler, C. T.; Tran, C. Q.; Paterson, D.; Cookson, D. J.; Barnea, Z. Monitoring Fluctuations at a Synchrotron Beamline Using Matched Ion Chambers: 2. Isolation of Component Noise Sources, and Application to Attenuation Measurements Showing Increased Precision by Two Orders of Magnitude. *X-Ray Spectrom.* **2000**, *29*, 459–466.
- (18) Tröger, L.; Arvanitis, D.; Baberschke, K.; Michaelis, H.; Grimm, U.; Zschech, E. Full correction of the self-absorption in soft-fluorescence extended x-ray-absorption fine structure. *Phys. Rev. B* **1992**, *46*, 3283–3289.
- (19) Pfalzer, P.; Urbach, J.-P.; Klemm, M.; Horn, S.; DenBoer, M.; Frenkel, A.; Kirkland, J. Elimination of self-absorption in fluorescence hard-x-ray absorption spectra. *Phys. Rev. B* **1999**, *60*, 9335–9339.
- (20) Eisebitt, S.; BBoske, T.; Rubensson, J. E.; Eberhardt, W. Determination of absorption coefficients for concentrated samples by fluorescence detection. *Phys. Rev. B* **1993**, *47*, 14103–14109.
- (21) Lamberti, C.; Bokhoven, J. A. *X-ray Absorption and X-ray Emission Spectroscopy*; Bokhoven, J. A.; Lamberti, C., Eds.; Wiley, 2016; pp 353–375.
- (22) Islam, M. T.; Best, S. P.; Bourke, J. D.; Tantau, L. J.; Tran, C. Q.; Wang, F.; Chantler, C. T. Accurate X-ray absorption spectra of dilute systems: Absolute measurements and structural analysis of ferrocene and decamethylferrocene. *J. Phys. Chem. C* **2016**, *120*, 9399–9418.
- (23) Fornasini, P. *Synchrotron Radiation, Basics, Methods and Applications*; Mobilio, S.; Boscherini, F.; Meneghini, C., Eds.; Springer-Verlag, 2015; pp 181–211.
- (24) Boscherini, F. *X-ray Absorption Spectroscopy of Semiconductors*; Schnohr, C. S.; Ridgeway, M. C., Eds.; Springer, 2015; p 77.
- (25) Ramaker, D. E. *X-ray Absorption and X-ray Emission Spectroscopy*; Bokhoven, J. A.; Lamberti, C., Eds.; Wiley, 2016; pp 485–522.
- (26) Krappe, H. J.; Rossner, H. H. Bayes-Turchin Approach to x-ray Absorption Fine Structure Data Analysis. *Phys. Rev. B* **2002**, *66*, No. 184303.
- (27) Bourke, J. D.; Chantler, C. T.; Witte, C. Finite difference method calculations of X-ray absorption fine structure for copper. *Phys. Lett. A* **2007**, *360*, 702–706.
- (28) Kas, J. J.; Rehr, J. J.; Glover, J.; Chantler, C. T. Comparison of theoretical and experimental Cu and Mo K-edge XAS. *Nucl. Instrum. Methods Phys. Res., Sect. A* **2010**, *619*, 28–32.
- (29) Chantler, C. T.; Bourke, J. D. Full-potential theoretical investigations of electron inelastic mean free paths and extended x-ray absorption fine structure in molybdenum. *J. Phys.: Condens. Matter* **2014**, *26*, No. 145401.
- (30) Bourke, J. D.; Islam, M. T.; Best, S. P.; Tran, C. Q.; Wang, F.; Chantler, C. T. Conformation Analysis of Ferrocene and Decamethylferrocene via Full-Potential Modeling of XANES and XAFS Spectra. *J. Phys. Chem. Lett.* **2016**, *7*, 2792–2796.
- (31) Boyanov, B. I.; Bunker, G.; Morrison, T. I. Analysis of EXAFS Data from Mixed-Shell Systems. *J. Synchrotron Radiat.* **1996**, *3*, 120–128.
- (32) Lin, S.-L.; Stern, E. A.; Kalb, A. J.; Zhang, Y. X-ray Absorption Fine Structure Investigation of the Zinc Transition Metal Binding Site of Zn Concanavalin A in Solution and in the Crystal. *Biochemistry* **1991**, *30*, 2323–2332.
- (33) Stern, E. A. Number of Relevant Independent Points in x-ray Absorption Fine Structure Spectra. *Phys. Rev. B* **1993**, *48*, 9825–9827.
- (34) Krappe, H. J.; Rossner, H. H. Error Analysis of EXAFS Measurements. *Phys. Rev. B* **2000**, *61*, 6596–6610.
- (35) Rehr, J. J.; Kozdon, J.; Kas, J.; Krappe, H. J.; Rossner, H. H. Bayes-Turchin Approach to XAS Analysis. *J. Synchrotron Radiat.* **2005**, *12*, 70–74.
- (36) Newville, M. EXAFS Analysis Using FEFF and FEFFIT. *J. Synchrotron Radiat.* **2001**, *8*, 96–100.
- (37) Newville, M. IFEFFIT: Interactive XAFS analysis and FEFF fitting. *J. Synchrotron Radiat.* **1998**, *8*, 322–324.
- (38) Ravel, B. *X-ray Absorption and X-ray Emission Spectroscopy*; Bokhoven, J. A.; Lamberti, C., Eds.; Wiley, 2016; pp 281–302.
- (39) Calvin, S. *XAFS for Everyone*; CRC Press: New York, 2013.
- (40) Stern, E. A.; Livins, P.; Zhang, Z. Thermal Vibration and Melting from a Local Perspective. *Phys. Rev. B* **1991**, *43*, 8850–8860.
- (41) Filipponi, A. Statistical Errors in X-ray Absorption Fine-Structure Data Analysis. *J. Phys.: Condens. Matter* **1995**, *7*, 9343–9356.
- (42) Newville, M.; Kas, J. J.; Rehr, J. J. Improvements in Modeling EXAFS with Many-Pole Self-Energy and FEFF 8.5. *J. Phys.: Conf. Ser.* **2009**, *190*, No. 012023.
- (43) Teo, B. K.; Joy, D. C. *EXAFS Spectroscopy: Techniques and Applications*; Springer US: Plenum, NY, 1981; pp 13–59.
- (44) Kas, J. J.; Jorisson, K.; Rehr, J. J. *X-ray Absorption and X-ray Emission Spectroscopy*; Bokhoven, J. A.; Lamberti, C., Eds.; Wiley, 2016; pp 73–97.
- (45) Teo, B. K. *EXAFS: Basic Principles and Data Analysis*, 1st ed.; Springer-Verlag: Berlin, Heidelberg, 1986.